

## Article

# The Role of Cerium Valence in the Conversion Temperature of $\text{H}_2\text{Ti}_3\text{O}_7$ Nanoribbons to $\text{TiO}_2$ -B and Anatase Nanoribbons, and Further to Rutile

Polona Umek <sup>1,\*</sup> , Michael Dürrschnabel <sup>2</sup> , Leopoldo Molina-Luna <sup>3</sup>, Srečo Škapin <sup>1</sup> ,  
Romana Cerc Korošec <sup>4</sup>  and Carla Bittencourt <sup>5,\*</sup> 

<sup>1</sup> Jožef Stefan Institute, Jamova Cesta 39, 1000 Ljubljana, Slovenia; sreco.skapin@ijs.si

<sup>2</sup> Karlsruhe Institute of Technology, P.O. Box 6980, 706049 Karlsruhe, Germany; michael.duerrschnabel@kit.edu

<sup>3</sup> Department of Materials and Earth Sciences, Technische Universität Darmstadt, Peter-Grünberg-Strasse 2, 64287 Darmstadt, Germany; molina@aem.tu-darmstadt.de

<sup>4</sup> Faculty of Chemistry and Chemical Technology, University of Ljubljana, Večna Pot 113, 1000 Ljubljana, Slovenia; romana.cerc-lj.si

<sup>5</sup> Chimie des Interactions Plasma-Surface (ChIPS), Research Institute for Materials Science and Engineering, University of Mons, 7000 Mons, Belgium

\* Correspondence: polona.umek@ijs.si (P.U.); carla.bittencourt@umons.ac.be (C.B.)

**Abstract:**  $\text{CeO}_2$ - $\text{TiO}_2$  is an important mixed oxide due to its catalytic properties, particularly in heterogeneous photocatalysis. This study presents a straightforward method to obtain 1D  $\text{TiO}_2$  nanostructures decorated with  $\text{CeO}_2$  nanoparticles at the surface. As the precursor, we used  $\text{H}_2\text{Ti}_3\text{O}_7$  nanoribbons prepared from sodium titanate nanoribbons by ion exchange. Two cerium sources with an oxidation state of +3 and +4 were used to obtain mixed oxides. HAADF-STEM mapping of the  $\text{Ce}^{4+}$ -modified nanoribbons revealed a thin continuous layer at the surface of the  $\text{H}_2\text{Ti}_3\text{O}_7$  nanoribbons, while  $\text{Ce}^{3+}$  cerium ions intercalated partially between the titanate layers. The phase composition and morphology changes were monitored during calcination between 620 °C and 960 °C. Thermal treatment led to the formation of  $\text{CeO}_2$  nanoparticles on the surface of the  $\text{TiO}_2$  nanoribbons, whose size increased with the calcination temperature. The use of  $\text{Ce}^{4+}$  raised the temperature required for converting  $\text{H}_2\text{Ti}_3\text{O}_7$  to  $\text{TiO}_2$ -B by approximately 200 °C, and the temperature for the formation of anatase. For the  $\text{Ce}^{3+}$  batch, the presence of cerium inhibited the conversion to rutile. Analysis of cerium oxidation states revealed the existence of both +4 and +3 in all calcined samples, regardless of the initial cerium oxidation state.

**Keywords:**  $\text{TiO}_2$ ;  $\text{TiO}_2$ -B; anatase;  $\text{CeO}_2$ ; impregnation; ion exchange; transformation; calcination;  $\text{CeO}_2$ - $\text{TiO}_2$ ; mixed oxides



**Citation:** Umek, P.; Dürrschnabel, M.; Molina-Luna, L.; Škapin, S.; Korošec, R.C.; Bittencourt, C. The Role of Cerium Valence in the Conversion Temperature of  $\text{H}_2\text{Ti}_3\text{O}_7$  Nanoribbons to  $\text{TiO}_2$ -B and Anatase Nanoribbons, and Further to Rutile. *Molecules* **2023**, *28*, 5838. <https://doi.org/10.3390/molecules28155838>

Academic Editor: Marinella Striccoli

Received: 11 July 2023

Revised: 31 July 2023

Accepted: 1 August 2023

Published: 3 August 2023



**Copyright:** © 2023 by the authors. Licensee MDPI, Basel, Switzerland. This article is an open access article distributed under the terms and conditions of the Creative Commons Attribution (CC BY) license (<https://creativecommons.org/licenses/by/4.0/>).

## 1. Introduction

Titanium dioxide ( $\text{TiO}_2$ ), owing to its unique combination of properties, high chemical stability, and low cost, is one of the most investigated materials used in a wide range of applications [1–3]; due to its high refractive index, opacity, and brightness, it has been widely used as a white pigment in paints, coatings, and plastics [4]. It is a wide-gap semiconducting material with  $E_g \sim 3.2$  eV exhibiting photocatalytic activity. This property makes it useful in air and water purification, self-cleaning surfaces, and even hydrogen fuel production [5]. Due to its biocompatibility, it has been used as material for prostheses in dental, orthopedic, and osteosynthesis applications [6,7].

Several approaches were suggested to tune the  $\text{TiO}_2$  properties, including particle size, particle shape and surface modification, and doping, to mention a few [8,9]. In the case of particle size and shape modification, several synthetic approaches were proposed for the preparation of nanosized  $\text{TiO}_2$ , including sol-gel, hydrothermal and solvothermal synthesis, microemulsion [10], and co-precipitation methods [11–13]. One-dimensional

(1D) TiO<sub>2</sub> nanostructures, such as nanotubes, nanowires, and nanoribbons, can be prepared from 1D hydrogen titanates (H<sub>2</sub>Ti<sub>n</sub>O<sub>2n+1</sub>) by thermal treatment in air [14–16]. Each method has its advantages and disadvantages, and the choice of method will depend on the specific application and desired properties of the nanosized TiO<sub>2</sub> material. Doping of TiO<sub>2</sub> with various transition metals or lanthanide ions can improve its properties by increasing its visible light absorption, enhancing its photocatalytic activity, and improving its charge separation efficiency [1,17]. Among the rare earth elements, cerium has received attention as cerium doping enhances optical absorption in the visible region and inhibits the recombination rate of photo-generated carriers [18–22]. Additionally, doping with lanthanide ions can modify the band structure of TiO<sub>2</sub>, improving its electronic and optical properties, and as a result, affecting its catalytic properties [23,24].

1D hydrogen trititanate nanostructures, i.e., H<sub>2</sub>Ti<sub>3</sub>O<sub>7</sub>, have been exploited as an attractive precursor for the preparation of 1D TiO<sub>2</sub> nanostructures for three main reasons: (i) these materials are thermally unstable, and upon heating, they readily transform to TiO<sub>2</sub> [25–28], (ii) they can be prepared in several 1D morphologies, such as nanotubes (HTiNTs) [29–32], nanowires [33–35], and nanoribbons (HTiNRs) [15,36], and (iii) low cost and facile synthesis routes. Three TiO<sub>2</sub> polymorphs, TiO<sub>2</sub>-B, anatase, and rutile, can be obtained by the thermal treatment of H<sub>2</sub>Ti<sub>3</sub>O<sub>7</sub> in air [15,16,37]. At elevated temperatures, anatase irreversibly transforms to rutile [38]. The fragmentation of the nanoribbons accompanies this transformation. On the other hand, the transformations from H<sub>2</sub>Ti<sub>3</sub>O<sub>7</sub> to TiO<sub>2</sub>-B and further to anatase are topotactic reactions as the morphology is preserved due to structural similarities between these three structures [25,39,40]. The transformation of H<sub>2</sub>Ti<sub>3</sub>O<sub>7</sub> to TiO<sub>2</sub>-B is not a direct one; it occurs in several dehydration steps [25,41]. The transformation temperatures strongly depend on the starting H<sub>2</sub>Ti<sub>3</sub>O<sub>7</sub> morphology. For instance, for nanoribbons with diameters up to 300 nm and lengths ranging from 500 nm to several microns, the conversion temperature for TiO<sub>2</sub>-B is approximately 400 °C [15,42]. For nanotubes that are hollow structures with average outer diameters of 12 nm and an inner between 5 and 8 nm, less energy is required. They transform already at 250 °C [32,43]. By doping, in small quantities, the conversion temperatures can be significantly altered, as in the case of HTiNRs doped with 1.5 wt.% of Mn<sup>2+</sup>, where rutile was reported to appear at 700 °C [36].

There have been only a few reports on doping 1D titanate [44–46] and TiO<sub>2</sub> nanostructures [47] with cerium. In the report by Viana et al. [44], sodium titanate nanotubes were used as a support for decoration with CeO<sub>2</sub> particles; (NH<sub>4</sub>)<sub>2</sub>Ce(NO<sub>3</sub>)<sub>6</sub> was used as a cerium source. By an ion-exchange reaction, Ce<sup>4+</sup> ions replaced Na<sup>+</sup> ions between the titanate layers, and CeO<sub>2</sub> nanoparticles grew on the surface of the nanotubes. It was shown that this modification shifted the adsorption band toward the visible range. Marques et al. [45] evaluated the critical concentration of Ce<sup>4+</sup> in the aqueous solution at which CeO<sub>2</sub> nanoparticles started forming in the titanate nanotubes' surface. These authors showed the presence of cerium in oxidation states of +4 and +3; the latter was formed via reduction reactions in an aqueous solution of the Ce<sup>4+</sup> precursor. The Ce<sup>3+</sup> ions also led to the successful ion exchange of sodium ions [46]. CeO<sub>2</sub> coating of TiO<sub>2</sub> nanotubes obtained by an anodization process increased the bioactivity of titania, as reported in [47].

We prepared two sets of H<sub>2</sub>Ti<sub>3</sub>O<sub>7</sub> nanoribbons (HTiNRs): (i) in the first one, the surface of HTiNRs was coated with a thin continuous cerium-containing layer, while in the second, (ii) cerium ions intercalated between the titanate layers in a low amount via an ion exchange reaction. For impregnation/intercalation of HTiNRs, two cerium salts, as sources of Ce<sup>4+</sup> and Ce<sup>3+</sup>, respectively, (Ce(SO<sub>4</sub>)<sub>2</sub>·4H<sub>2</sub>O and Ce(NO<sub>3</sub>)<sub>3</sub>·6H<sub>2</sub>O), were chosen to evaluate the effects of the starting cerium valence on surface impregnation and/or intercalation between titanate layers. The impact of cerium valence (+4 and +3) on modifying H<sub>2</sub>Ti<sub>3</sub>O<sub>7</sub> nanoribbons and in converting H<sub>2</sub>Ti<sub>3</sub>O<sub>7</sub> to TiO<sub>2</sub>-B, and further to anatase and rutile, were investigated. H<sub>2</sub>Ti<sub>3</sub>O<sub>7</sub> nanoribbons were selected as a precursor of TiO<sub>2</sub> nanoribbons for transformation conducted by calcination for three reasons: (i) a 1D shape that is preserved until anatase formation, (ii) a transformation pathway going

through three TiO<sub>2</sub> crystallographic phases, and (iii) a layered structure enabling cation intercalation. The difference in the oxidation state of the initial cerium ions was found to be crucial for the HTiNRs modification; in the case of Ce<sup>4+</sup>, a thin continuous cerium-containing layer at the surface of the nanoribbons was formed, while for the Ce<sup>3+</sup>, cerium ions via an ion exchange reaction intercalated between the titanate layers in a small amount. The transformation of cerium-modified H<sub>2</sub>Ti<sub>3</sub>O<sub>7</sub> nanoribbons to TiO<sub>2</sub>-B, and then to anatase and rutile upon increasing the calcination temperature, between 400 °C and 960 °C, was monitored. The temperature required for the formation of TiO<sub>2</sub>-B for both ions was higher than for the non-cerium-modified nanoribbons. The formation of CeO<sub>2</sub> nanoparticles on the surface of 1D TiO<sub>2</sub> nanostructures in the same temperature range was observed. Cerium in oxidation states of +4 and +3 were observed in all cerium-containing samples, regardless of the starting oxidation state of cerium. Interestingly, the presence of cerium in anatase nanoribbons prepared with the Ce<sup>3+</sup> increased the temperature for the conversion to rutile.

## 2. Results and Discussion

Hydrogen titanate nanoribbons (HTiNRs), with an average width of 30–300 nm and length of 0.5–10 μm, were used as a precursor for surface impregnation/intercalation with cerium and further transformation to CeO<sub>2</sub>-TiO<sub>2</sub> NR composites via calcination in air. A characteristic scanning electron microscopy (SEM) image of obtained HTiNRs revealed a high nanoribbon content with a smooth surface (Figure S1). Their powder X-ray diffraction (XRD) pattern (Figure S2, bottom panel) corresponds to the pattern of H<sub>2</sub>Ti<sub>3</sub>O<sub>7</sub> as reported in the literature [15,27,37].

### 2.1. Characterization of H<sub>2</sub>Ti<sub>3</sub>O<sub>7</sub> Nanoribbons Impregnated/Intercalated with Cerium

Two cerium salts sources Ce(SO<sub>4</sub>)<sub>2</sub>·4H<sub>2</sub>O and Ce(NO<sub>3</sub>)<sub>3</sub>·6H<sub>2</sub>O were used to prepare two sets of HTiNRs impregnated/intercalated with cerium, Ce<sup>4+</sup>-HTiNRs, and Ce<sup>3+</sup>-HTiNRs, respectively. The impregnation of HTiNRs with the Ce<sup>4+</sup> precursor affected the color of the nanoribbons, which changed from white to pale yellow. While the change in color of Ce<sup>3+</sup>-HTiNRs was not visible to our eyes. The powder X-ray diffraction patterns (XRDs) (Figure 1a,b, bottom panels) matched those reported for layered trititanate, i.e., H<sub>2</sub>Ti<sub>3</sub>O<sub>7</sub> (Figure S2, bottom panel) [15,27,37].

The peak at ~10° in the XRDs of the titanate samples (Figures 1 and S2), i.e., HTiNRs, Ce<sup>3+</sup>-HTiNRs, and Ce<sup>4+</sup>-HTiNRs, arises from the layered trititanate structure and gives information about the interlayer distance [48]. For Ce<sup>3+</sup>-HTiNRs, a shift in this peak from 10.54° to 10.68° was observed (Figure S3), indicating the contraction of the interlayer distance. Due to the bigger size of cerium (III) than the hydronium ion, the interlayer distance was expected to increase [49]. Since cerium (III) is a trivalent ion and hydronium ion is monovalent, one Ce<sup>3+</sup> changes to three hydronium ions. Therefore, it might be assumed that only a smaller amount of hydronium ions was exchanged with Ce<sup>3+</sup> ions; the exchange of hydronium ions with cerium (III) ions resulted in the removal of the interlayer water and the formation of vacancies, which promoted the strengthening of the Ti-O bonds, resulting in contraction of the interlayer distance [45]. Conversely, no shift in the peak ~10° for Ce<sup>4+</sup>-HTiNRs was observed, which might be associated with the formation of Ce<sup>4+</sup> polynuclear species [50–53], which are too large to intercalate between the titanate layers. This is supported by scanning transmission electron microscopy–electron energy loss spectroscopy (STEM–EELS) analysis (Figure 2). A comparison of the elemental maps (Ti, O, and Ce) reveals that the nanoribbon surface is covered with a continuous ~4 nm thick cerium layer. As expected, the impregnation of HTiNRs with Ce<sup>4+</sup> and Ce<sup>3+</sup> did not affect either the material's morphology or the surface of the NRs, which appears smooth, as revealed by SEM investigation (Figure S4).

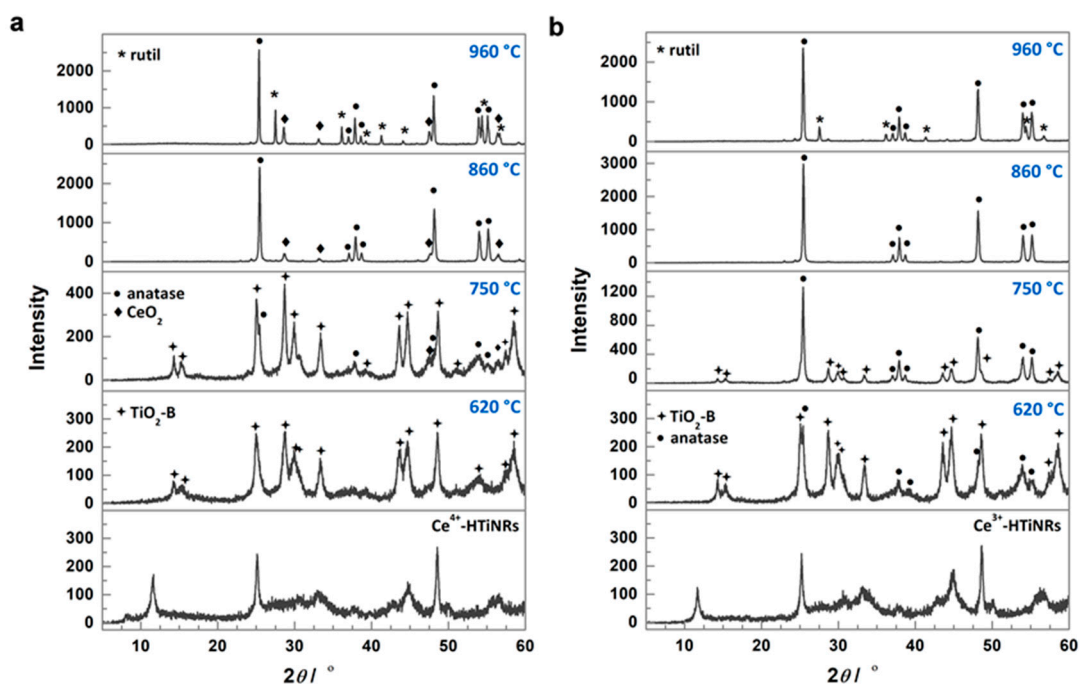


**Figure 1.** Impact of cerium oxidation state in the starting cerium source on the transformation temperature of  $\text{H}_2\text{Ti}_3\text{O}_7$  nanoribbons. XRD patterns of the precursor materials  $\text{Ce}^{4+}$ -HTiNRs (a) and  $\text{Ce}^{3+}$ -HTiNRs (b), and products obtained by calcination in air at 620, 750, 860, and 960 °C.

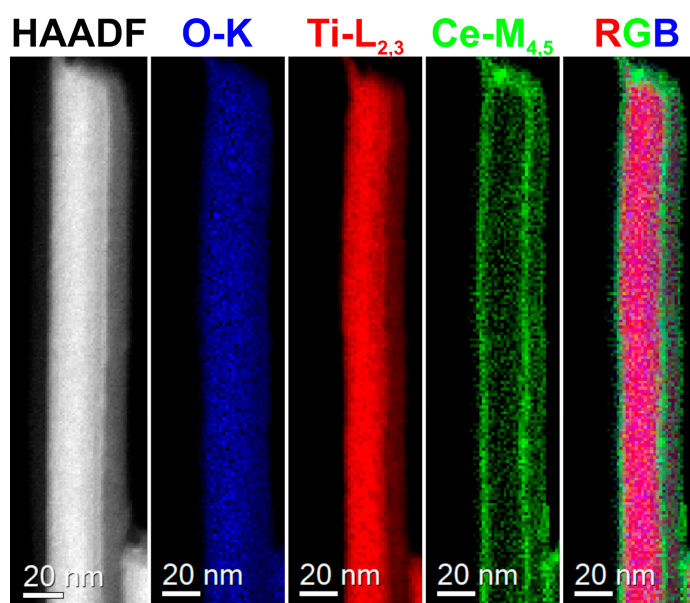


**Figure 2.** HAADF-STEM image of an individual  $\text{Ce}^{4+}$ -HTiNRs with corresponding elemental maps of Ti, O, Ce (EELS), and an RGB image.

The amount of cerium salts used for wet impregnation was calculated to give around 5 wt.% of cerium in the final product, that is,  $\text{TiO}_2$  NRs. The cerium content in  $\text{Ce}^{4+}$ -HTiNRs, determined with energy dispersive X-ray spectroscopy (EDXS) analysis, is 3.4 wt.% and 0.3 wt.% for  $\text{Ce}^{4+}$ -HTiNRs and  $\text{Ce}^{3+}$ -HTiNR, respectively (Table 1).

**Table 1.** Sample labels, transformation conditions, phase composition, cerium content, oxidation state, and band gap values.

Sample Labels	Precursor	Transformation Environment	T (°C)	Phase Composition	Ce CONTENT <sup>a</sup> (wt.%)	Ce Oxidation State <sup>b</sup>	Band Gap (eV)
Ce <sup>4+</sup> -HTiNRs	H <sub>2</sub> Ti <sub>3</sub> O <sub>7</sub> NRs	DI water <sup>c</sup>	100	H <sub>2</sub> Ti <sub>3</sub> O <sub>7</sub>	3.4	+3, +4 (80%)	3.56
Ce <sup>4+</sup> -620 °C	Ce <sup>4+</sup> -HTiNRs	static air	620	TiO <sub>2</sub> -B	3.9	+3, +4 (75%)	3.30
Ce <sup>4+</sup> -750 °C	Ce <sup>4+</sup> -HTiNRs	static air	750	TiO <sub>2</sub> -B, anatase	3.9	+3, +4 (70%)	3.17
Ce <sup>4+</sup> -860 °C	Ce <sup>4+</sup> -HTiNRs	static air	860	anatase	3.8	+3, +4 (50%)	3.27
Ce <sup>4+</sup> -960 °C	Ce <sup>4+</sup> -HTiNRs	static air	960	anatase, rutile	3.7	+3, +4 (50%)	3.19
Ce <sup>3+</sup> -HTiNRs	H <sub>2</sub> Ti <sub>3</sub> O <sub>7</sub> NRs	DI water <sup>b</sup>	100	H <sub>2</sub> Ti <sub>3</sub> O <sub>7</sub>	0.2	+3, +4	3.53
Ce <sup>3+</sup> -620 °C	Ce <sup>3+</sup> -HTiNRs	static air	620	TiO <sub>2</sub> -B, anatase	0.3	+3, +4	3.40
Ce <sup>3+</sup> -750 °C	Ce <sup>3+</sup> -HTiNRs	static air	750	anatase, traces of TiO <sub>2</sub> -B	0.3	+3, +4	3.36
Ce <sup>3+</sup> -860 °C	Ce <sup>3+</sup> -HTiNRs	static air	860	anatase	0.3	+3, +4	3.34
Ce <sup>3+</sup> -960 °C	Ce <sup>3+</sup> -HTiNRs	static air	960	anatase, rutile	0.4	+3, +4	3.31
HTiNRs	/	/	/	H <sub>2</sub> Ti <sub>3</sub> O <sub>7</sub>	/	/	3.46
<sup>d</sup> p-620 °C	H <sub>2</sub> Ti <sub>3</sub> O <sub>7</sub> NRs	static air	620	anatase, traces of TiO <sub>2</sub> -B	/	/	3.31
p-750 °C	H <sub>2</sub> Ti <sub>3</sub> O <sub>7</sub> NRs	static air	750	anatase	/	/	3.28
p-860 °C	H <sub>2</sub> Ti <sub>3</sub> O <sub>7</sub> NRs	static air	860	anatase	/	/	3.29
p-960 °C	H <sub>2</sub> Ti <sub>3</sub> O <sub>7</sub> NRs	static air	960	anatase, rutile	/	/	3.01

<sup>a</sup> cerium content was determined by EDXS–SEM; <sup>b</sup> cerium oxidation state was determined using XPS (for Ce<sup>3+</sup>-modified nanoribbons; due to the small relative amount of cerium, it was impossible to evaluate the ratio between Ce<sup>3+</sup>/Ce<sup>4+</sup> oxidation states) and <sup>c</sup> deionized water. <sup>d</sup> p, pristine is used to label samples not doped with cerium.

Results of thermo-gravimetric analysis (TGA) of both Ce-containing HTiNR samples (Figure S5) are similar to the TGA curve of pure HTiNRs [15]. However, a slightly higher weight loss (1.1 wt.%) was observed for the HTiNRs impregnated with Ce<sup>4+</sup>, which can be explained by a higher cerium content (Table 1) [51–53].

## 2.2. Conversion of H<sub>2</sub>Ti<sub>3</sub>O<sub>7</sub> Nanoribbons to TiO<sub>2</sub> by Thermal Treatment in Air

Based on a preliminary study, the calcination temperatures were set to 620 °C, 750 °C, 860 °C, and 960 °C. In addition, a batch of samples obtained by calcination of pristine HTiNRs for the comparison of phase composition and morphology was prepared. Sample labels, calcination temperatures, phase compositions, cerium contents, cerium oxidation states, and band gap values are listed in Table 1.

### 2.2.1. Cerium Content

The cerium content of the calcined samples, obtained with EDXS analysis, is given in Table 1. At the final calcination temperature of 960 °C, the cerium content is 3.7 and 0.4 wt.% for Ce<sup>4+</sup> and Ce<sup>3+</sup> products, respectively. Small amounts of sulfur were detected in the samples obtained by calcinating the Ce<sup>4+</sup>-HTiNRs. The sulfate group in the cerium precursor fully decomposed only above 800 °C. In comparison, the decomposition of the nitrate group of the source Ce(NO<sub>3</sub>)<sub>3</sub>·6H<sub>2</sub>O occurs before reaching 300 °C (Figures S6 and S7).

### 2.2.2. Structural Determination of TiO<sub>2</sub> Polymorphs

The XRD pattern of the pristine HTiNRs (H<sub>2</sub>Ti<sub>3</sub>O<sub>7</sub> NRs) sample calcined at 620 °C shows the presence of the anatase phase (ICCD card no. 86-1157) and traces of TiO<sub>2</sub>-B (ICCD card no. 35-0088); the transformation to anatase was completed at 860 °C. With an increased calcination temperature to 960 °C, in addition to anatase related peaks, new peaks corresponding to rutile (ICCD card no. 89-0555) appeared (Figure S2). For pristine HTiNRs, the transformation to TiO<sub>2</sub>-B was reported to occur typically at 400 °C [15,42]. While for the complete conversion of Ce<sup>4+</sup>-HTiNRs to TiO<sub>2</sub>-B, a higher temperature (620 °C) was required (Figure 1a). As the temperature was raised to 750 °C, TiO<sub>2</sub>-B partly converted to anatase, and new peaks corresponding to CeO<sub>2</sub> appeared (ICCD card no. 81-0792). Transformation to anatase was completed at 860 °C; all peaks in the Ce<sup>4+</sup>-860 °C diffractogram

corresponded to anatase and CeO<sub>2</sub>. With a further increase in the calcination temperature to 960 °C, anatase partially converted to rutile. In the case of the Ce<sup>3+</sup>-HTiNRs precursor (Figure 1b), at 620 °C, the main phase was TiO<sub>2</sub>-B with traces of anatase. At 750 °C, almost all TiO<sub>2</sub>-B is converted to anatase. Similar to the Ce<sup>4+</sup>-HTiNR batch, the transformation to anatase was completed at 860 °C. In Ce<sup>3+</sup>-HTiNRs, anatase was partially converted to rutile as the temperature was raised to 960 °C (Figure 1b).

Next, from the intensities of the (101) anatase and (110) rutile peaks (Figures 1a,b and S2), positioned at ~25.3° and 27.4°, respectively, for the samples calcined at 960 °C the amount of rutile was calculated using the equation suggested by Spurr and Mayers [54] (Table 2). In p-960 °C, rutile was already the majority phase (60 wt.%), while in Ce<sup>4+</sup>-960 °C and Ce<sup>3+</sup>-960 °C, the amount of rutile was 31% and 17%, respectively. This might suggest that the cerium source and location of cerium ions in anatase nanoribbons may play an essential role in inhibiting the transformation to rutile. Therefore, regardless of the cerium source and content, the presence of cerium in HTiNRs, i.e., Ce<sup>3+</sup>-HTiNRs and Ce<sup>4+</sup>-HTiNRs (Table 1), significantly raised the temperature for both transformations, TiO<sub>2</sub>-B to anatase and anatase to rutile, when compared to the pristine HTiNRs (Figure S2) [15,42,55], or as reported to Mn<sup>2+</sup>-doped HTiNRs [36], where rutile had already appeared below 600 °C.

**Table 2.** The wt.% of rutile in the samples calcined at 960 °C.

Sample	wt.% Rutile
Ce <sup>4+</sup> -960 °C	31
Ce <sup>3+</sup> -960 °C	17
p-960 °C	60

In addition, the size of CeO<sub>2</sub> nanoparticles was calculated from the (111) CeO<sub>2</sub> peak positioned at 28.7° (ICDD card no. 81-0792) using the Scherer formula ( $d = 0.9 \lambda / B \cos \theta$ ;  $\lambda = 1.54 \text{ \AA}$ , where B is the full width at half maximum and is the Bragg angle). The calculated values are 22 nm and 33 nm for Ce<sup>4+</sup>-860 °C and Ce<sup>4+</sup>-960 °C, respectively.

### 2.2.3. Changes in the Nanoribbon Morphology and Formation of CeO<sub>2</sub> Nanoparticles

Figure S8 summarizes the impact of the calcination temperature on changes in the nanoribbons' shape for samples prepared by calcination of Ce<sup>4+</sup>-HTiNRs. As expected, the nanoribbon morphology was intact until 750 °C. At 860 °C, the diameter along individual nanoribbons was no longer uniform. At some places along the nanoribbons, thicker areas appeared, and the nanoribbon edges became rounder due to the sintering effect. At 960 °C, the observed elongated structures were much thicker (Figure S8d) than the starting nanoribbons [42]; it looked as if the elongated thickened parts, originating from the nanoribbons, formed a kind of three-dimensional network. In addition, as expected, the fragmentation of nanoribbons, caused by the anatase to rutile transformation, was more severe for p-960 °C (Figure S9) due to a higher mass fraction of rutile compared to Ce<sup>4+</sup>-960 °C and Ce<sup>3+</sup>-960 °C (Table 2). Interestingly, the nanoribbon morphology was less affected in Ce<sup>3+</sup>-960 °C than in Ce<sup>4+</sup>-960 °C, which is associated with a lower amount of rutile in the former (Table 2), suggesting that cerium species in Ce<sup>3+</sup>-960 °C inhibited the conversion to rutile. Similar findings were observed when CeO<sub>2</sub> was added to the CuO-TiO<sub>2</sub> system [56].

Upon calcination, CeO<sub>2</sub> nanoparticles were observed on the surface of the TiO<sub>2</sub> nanoribbons (NPs) (Figure 3); for the Ce<sup>4+</sup> batch, they were observed (in SEM images) at 750 °C, while for the Ce<sup>3+</sup> batch, they were observed at 860 °C. The difference in the temperature at which CeO<sub>2</sub> NPs start to be observed can be associated with the cerium content, which was much lower for the Ce<sup>3+</sup> batch (Table 1), and the fact that cerium ions in Ce<sup>3+</sup>-HTiNRs intercalated between the titanate layers needed more to migrate to the surface. Upon a higher calcination temperature, cerium atoms between the layers diffuse toward the surface, where they segregate, forming CeO<sub>2</sub> NPs [56]. Therefore, we

decided to investigate the sample calcined at the lowest temperature ( $\text{Ce}^{4+}$  batch) in more detail. STEM-EDX elemental mapping of  $\text{Ce}^{4+}$ -620 °C revealed a small number of cerium-containing nanoparticles with diameters below 20 nm on the surface of the nanoribbons (Figure S11).

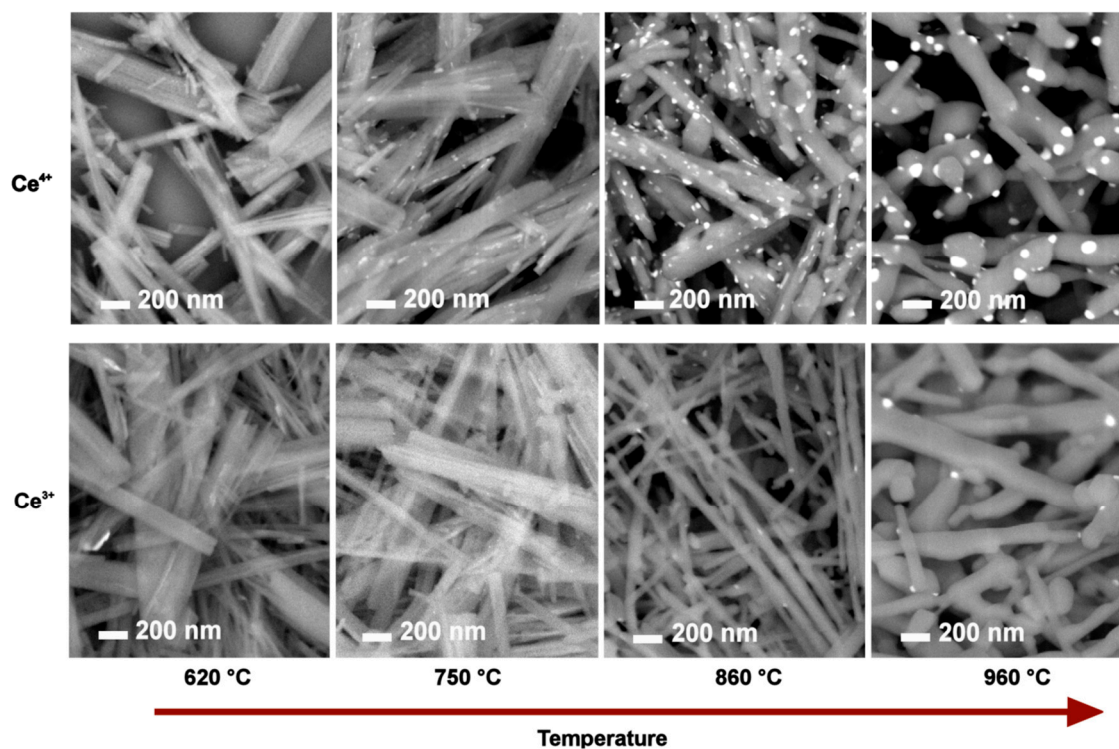


**Figure 3.** Evolution of  $\text{CeO}_2$  nanoparticles on the surface of  $\text{TiO}_2$  nanoribbons and fragmentation of nanoribbon morphology with increasing calcination temperatures for  $\text{Ce}^{4+}$ -HTiNRs (**top**) and  $\text{Ce}^{3+}$ -HTiNRs (**bottom**), which were calcined at 620 °C, 750 °C, 860 °C, and 960 °C. SEM images using a back-scattered electron detector were taken at the same magnification. Areas with  $\text{CeO}_2$  nanoparticles in the images appear brighter.

With the increasing calcination temperature, the  $\text{CeO}_2$  NP size increased. The density distribution of  $\text{CeO}_2$  NPs was higher at the final calcination temperature (960 °C) for the  $\text{Ce}^{4+}$  sample than for the  $\text{Ce}^{3+}$  sample due to a higher cerium content (Table 1). The measured diameter of  $\text{CeO}_2$  NPs was between 13 and 35 nm for  $\text{Ce}^{4+}$ -850 °C, while in  $\text{Ce}^{4+}$ -960 °C, their size was between 20 and 70 nm (Figure S10), which agreed with the calculated values from the XRDs.

#### 2.2.4. Determination of Cerium Oxidation State and the Ratio between $\text{Ce}^{4+}/\text{Ce}^{3+}$

$\text{CeO}_2$  is known for its unique redox chemistry. Oxidation states +3 and +4 steadily exist and can easily switch between each other [57,58]. Therefore,  $\text{Ce}^{4+}$ -620 °C was investigated by STEM-EELS measurements to determine the cerium valence, at a nanoparticle and at a region of a nanoribbon without a particle. (Figure S11). The results are shown in Figure 4; the circles in the high-angle annular dark-field (HAADF) image denote the exact locations from which the electron energy loss (EEL) spectra of the  $\text{Ce-M}_{4,5}$  were measured (Figure 4a,b). In the EEL spectrum measured over the nanoparticle beside the  $M_4$  and  $M_5$  edges, the post-edge peaks associated with  $\text{Ce}^{4+}$  appeared. The  $M_4$  and  $M_5$  edges in the spectrum measured at the nanoribbon shifted to a lower energy loss by 1.6 and 1.1 eV, respectively, which is characteristic of  $\text{Ce}^{3+}$ . Therefore, we can conclude that cerium at the surface of the nanoribbon was a mixture of  $\text{Ce}^{4+}$  and  $\text{Ce}^{3+}$ , and in the nanoparticle, it is more  $\text{Ce}^{4+}$ .

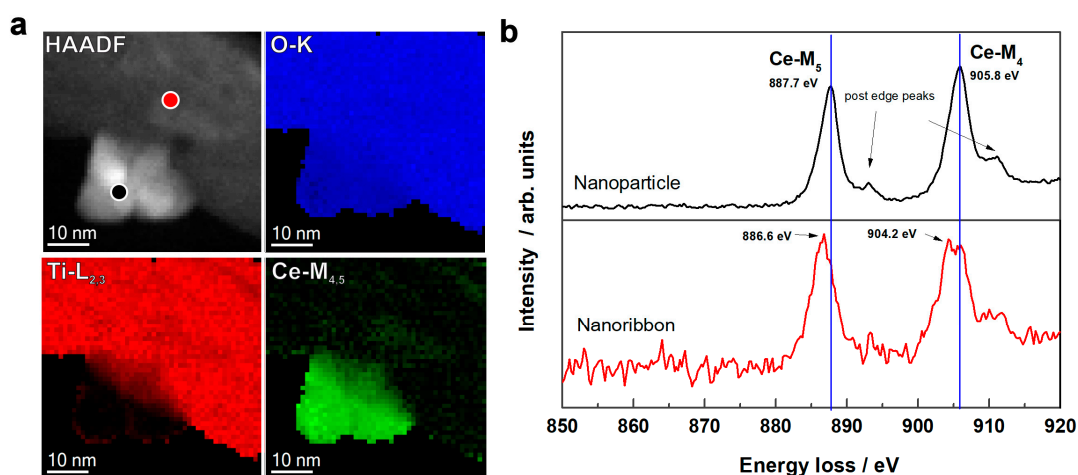


**Figure 4.** STEM–EELS analysis of sample  $\text{Ce}^{4+}$ -620 °C. (a) HAADF image with corresponding elemental maps of O, Ti, and Ce. (b) EEL spectra recorded at the nanoribbon surface (red spot in the HAADF image) and a particle attached to the surface of the nanoribbon (black spot in the HAADF image).

X-ray photoelectron spectroscopy (XPS) was used to probe a larger sample area to determine the cerium oxidation states and their ratios in the samples derived by the calcination of  $\text{Ce}^{4+}$ -HTiNRs (Table 1 and Figure 5). In all samples obtained from  $\text{Ce}^{4+}$ -HTiNRs, the presence of cerium in oxidation states +4 and +3 was observed, which is not surprising given the facile transformation of  $\text{Ce}^{4+}$  to  $\text{Ce}^{3+}$  [57]. In the Ce 3d core level region of the XPS spectra, several characteristic structures of  $\text{CeO}_2$  appeared for annealing at higher temperatures; the main peak is centered at 915 eV and the shoulder at 880 eV of binding energy (Figure 5a,b). The intensity of both structures increased with increasing calcination temperatures, indicating that the amount of  $\text{CeO}_2$  increased, which coincides well with the XRD analysis (Figure 1a and Figure S10). Due to the low cerium content in materials derived from  $\text{Ce}^{3+}$ -HTiNRs (Table 1), evaluation of the ratio of  $\text{Ce}^{3+}/\text{Ce}^{4+}$  in these materials was impossible due to the low quality of the spectra; however, the peak structures characteristics for both cerium oxidation states could be observed (Figure 5c).

#### 2.2.5. Optical Band Gap Features

The last column in Table 1 reports the band gap energies of all three sets of samples. The band gap of HTiNRs is 3.45 eV. Surprisingly, the band gap energies of  $\text{Ce}^{4+}$ -HTiNRs and  $\text{Ce}^{3+}$ -HTiNRs are slightly higher, 3.56 and 3.53 eV, respectively. This might be connected with (i) the presence of sodium ions in trace amounts [5] left between the layers after ion exchange (the amount of sodium in HTiNRs determined with EDXS analysis was below the detection limit of 0.1 wt.%), and/or (ii) with the presence of a thin Ce-containing layer on the surface of  $\text{Ce}^{4+}$ -HTiNRs, and (iii) reduced order due to partial exchange of hydronium ions by  $\text{Ce}^{3+}$  in the case of  $\text{Ce}^{3+}$ -HTiNRs [59]. During thermal treatment in air, the  $E_g$  was gradually reduced with increasing calcination temperatures for all three sets of samples. This can be attributed to the formation of  $\text{TiO}_2$ -B, anatase, and rutile (for the highest calcination temperature), and to the increasing crystallinity (Figures 1a,b and S1) of the nanoribbons.

Reported band gap energies of crystalline bulk  $\text{TiO}_2$ -B and anatase are equal, namely, 3.2 eV [5], and are smaller than those measured for our  $\text{TiO}_2$  samples (Table 1). During the particle size reduction from micro to nano-sized particles, the band gap values of semiconductors are usually increased [60].

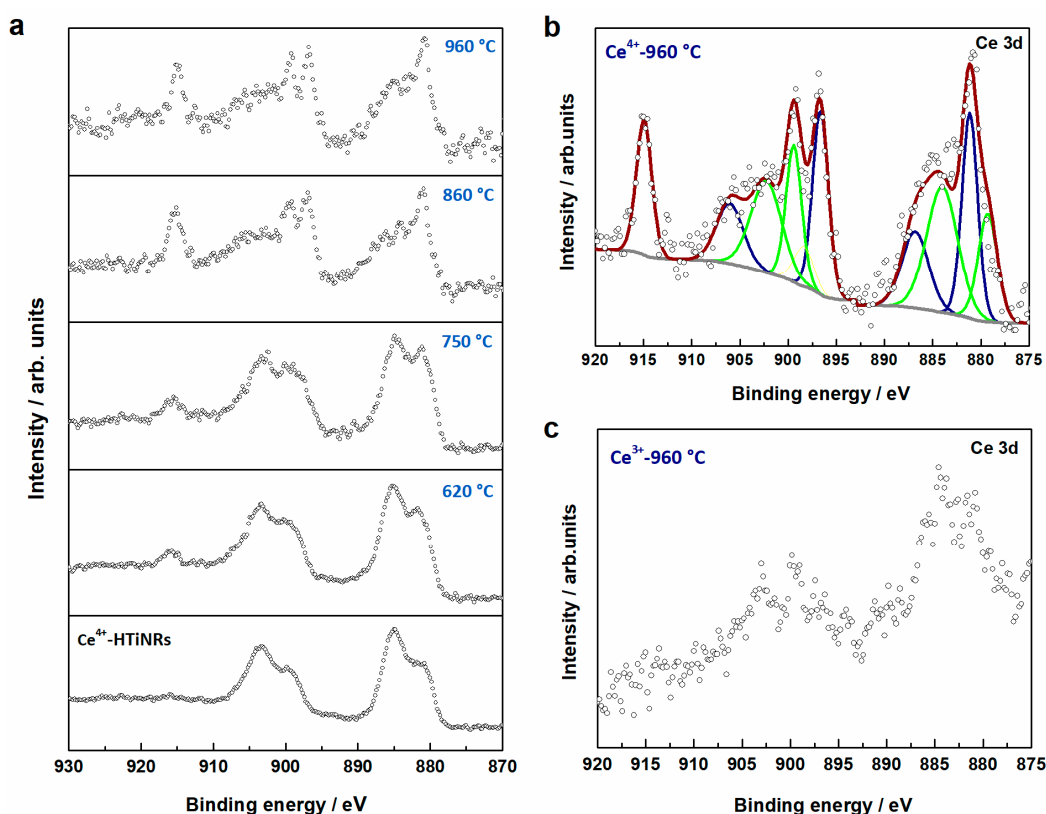


**Figure 5.** (a) Comparison of X-ray photoelectron spectra recorded in the Ce 3d core level region for Ce<sup>4+</sup>-HTiNRs and products obtained after calcination at 620 °C, 750 °C, 860 °C, and 960 °C. (b) Result of the peak fitting in the Ce 3d core level X-ray photoelectron spectrum of the sample calcined at 960 °C; green peaks refer to Ce<sup>3+</sup> and blue ones to Ce<sup>4+</sup>. (c) Spectrum of Ce<sup>3+</sup>-960 °C in the Ce 3d core level region.

### 3. Materials and Methods

#### 3.1. Materials Preparation

**Preparation of H<sub>2</sub>Ti<sub>3</sub>O<sub>7</sub> nanoribbons.** The starting material, H<sub>2</sub>Ti<sub>3</sub>O<sub>7</sub> nanoribbons (NRs), were prepared according to the method already reported elsewhere [15,61], with the exception that for the preparation of H<sub>2</sub>Ti<sub>3</sub>O<sub>7</sub> NRs from (Na, H)<sub>2</sub>Ti<sub>3</sub>O<sub>7</sub> NRs by ion exchange, instead of 0.1 M CH<sub>3</sub>COOH, 0.1 M HCl were used [36].

**Preparation of TiO<sub>2</sub> NRs decorated with CeO<sub>2</sub> NPs via calcination in air.** Firstly, a wet impregnation was employed to prepare H<sub>2</sub>Ti<sub>3</sub>O<sub>7</sub> NRs coated with cerium. As precursors of cerium in oxidation states +4 and +3, Ce(SO<sub>4</sub>)<sub>2</sub>·4H<sub>2</sub>O and Ce(NO<sub>3</sub>)<sub>3</sub>·6H<sub>2</sub>O were used. The amount of cerium precursors was calculated to give approximately 5 wt.% of cerium in TiO<sub>2</sub> NRs; in brief, 1 g of HTiNRs was dispersed into 120 mL of deionized water, then 50 mL of a water solution of cerium precursor (120 mg of Ce(SO<sub>4</sub>)<sub>2</sub>·4H<sub>2</sub>O and 135 mg of Ce(NO<sub>3</sub>)<sub>3</sub>·6H<sub>2</sub>O) was added dropwise. Prepared mixtures were stirred overnight, then filtrated, and finally dried in air at 100 °C for 10 h. Prepared precursors were labeled Ce<sup>4+</sup>-HTiNRs and Ce<sup>3+</sup>-HTiNRs. In the next step, H<sub>2</sub>Ti<sub>3</sub>O<sub>7</sub> nanoribbons impregnated with cerium were transformed into TiO<sub>2</sub> NRs decorated with CeO<sub>2</sub> nanoparticles (NPs) by calcination in static air; 150 mg of the precursor was weighed in an alumina boat, placed into an oven (Carbolite), and heated to the target temperature (400 °C, 620 °C, 750 °C, 860 °C, and 960 °C) at 1 °C/min. Samples were maintained at the selected temperature for 7 h and then cooled to room temperature. Sample labels, exact reaction conditions, and phase compositions are listed in Table 1.

### 3.2. Materials Characterization

The physical and chemical properties of the prepared materials were analyzed using several experimental techniques. The morphological features were studied using field emission scanning electron microscopes (SEM) (JEOL-7600F, JEOL Tokyo, Japan and Verios G4, ThermoFischer, Waltham, MA, USA) and a transmission electron microscope (HRTEM), JEM 2100 (Jeol Ltd., Akishima City, Japan). Specimens for the SEM analysis were prepared by dispersing a small amount of prepared powder samples in deionized water, and a drop of the dispersion was deposited on a polished surface of an Al sample holder. Before the SEM investigation, a ca. 3 nm thick carbon layer was deposited on the specimens to reduce the charging effect. The crystallinity of the nanoribbons and cerium distribution over the nanoribbons in the samples were investigated with a transmission electron microscope (TEM) Jeol 2100 at 200 keV and a ThermoFisher Talos F200X scanning transmission electron microscope (STEM) equipped with four energy-dispersive X-ray (EDX) detectors and a Gatan Enfium electron energy-loss (EEL) spectrometer (Gatan, Pleasanton, CA, USA) with DualEELS capability. The microscope was operated at 200 kV, and the energy resolution of the recorded EEL spectra was about 1.2 eV. The convergence and the collection angle for the EELS experiments were 10.5 and 14.1 mrad, respectively. The Ce M5/M4 ratio was determined using the second derivative method described in [62,63]. Specimens for TEM/HAADF-STEM analyses were dispersed ultrasonically in methanol, and a drop of the dispersion was deposited onto a lacy carbon film supported by a copper grid.

Identification of the phase composition of the samples was determined from powder X-ray diffraction (XRD) patterns measured using a D4 Endeavor, Bruker AXS diffractometer, Bruker, Karlsruhe, Germany with Cu K $\alpha$  radiation ( $\lambda = 1.5406 \text{ \AA}$ ) and a Sol-X energy-dispersive detector. Diffractograms were measured in the  $2\theta$  angular range with a step size of  $0.02^\circ \text{ s}^{-1}$  and a collection time of 3 s.

Elemental composition was determined from energy-dispersive X-ray data (EDX) measured using a field emission scanning electron microscope (JEOL 7600F) equipped with an EDX spectrometer elemental analysis system. Specimens for EDX analyses were prepared by pressing powder samples into pellets and placing them on carbon tape on an Al sample holder. The holder with the samples was coated with a thin carbon layer before the analysis.

X-ray spectroscopy (XPS) measurements have been conducted to determine the oxidation states of cerium and titanium. XPS measurements were performed with a VER-SAPROBE PHI 5000 (Physical Electronics, Inc., Chanhassen, MN, USA) equipped with a monochromatic Al K $\alpha$  X-ray source. The energy resolution was 0.7 eV. Specimens for XPS measurements were prepared by pressing the sample powders into pellets. A conductive double-face tape UHV compatible was used to attach the pellet to a sample holder.

Diffuse reflectance UV-Vis spectroscopy was used to obtain the energy gap value of the synthesized samples. The spectra were recorded using a UV-Vis-NIR spectrometer (Shimadzu UV-3600, Tokyo, Japan) equipped with an integrating sphere (ISR-3100, 60 mm) and BaSO $_4$  as a reference in the wavelength range of 200 to 800 nm with a 0.5 nm step size and a UV/Vis/NIR spectrometer (PerkinElmer Lambda 950, Hong Kong, China) equipped with a 150-nm sphere. The Kubelka-Munk function was applied to convert the diffuse reflectance into the absorbance [64]. The optical band-gap energy ( $E_g$ ) was determined from the wavelength at which the tangent of the absorbance line intersected the abscissa coordinate.

Thermal decomposition of Ce(SO $_4$ ) $_2$ ·4H $_2$ O was studied using a Mettler Toledo TGA/DSC 1 instrument from room temperature to 900 °C under dynamic airflow (50 mL min $^{-1}$ ). The heating rate was 10 °C min $^{-1}$ . Crystalhydrate with an initial mass of 5.124 mg was placed into a 150  $\mu$ L alumina crucible. The blank curve was automatically subtracted. Evolved gases were transferred to a mass spectrometer (Pfeiffer Vacuum ThermoStar) via the 75 cm long heated transfer line. For Ce $^{4+}$ -HTiNRs, Ce $^{3+}$ -HTiNRs, and Ce(SO $_4$ ) $_2$ ·4H $_2$ O, the same experimental parameters were used for TGA/DSC measurements as previously described. In the case of Ce(NO $_3$ ) $_3$ ·6H $_2$ O, where we were interested in

the DSC signal, a higher initial mass (19.129 mg) was used, while for Ce<sup>4+</sup>-HTiNRs and Ce<sup>3+</sup>-HTiNRs, the initial mass of the sample was around 5 mg. For these three samples, the upper temperature of measurements was 600 °C. The volume of platinum crucibles used was 150 µL.

#### 4. Conclusions

The surface of HTiNRs dispersed in a Ce<sup>4+</sup> aqueous solution was successfully impregnated with a thin 2–4 nm thick continuous cerium-containing layer. When Ce<sup>3+</sup> was used as the cerium source, ion exchange was more favorable; however, only a small amount of hydronium ions exchanged with the cerium ions. Upon calcination, CeO<sub>2</sub>-TiO<sub>2</sub> mixed oxide was formed. CeO<sub>2</sub> nanoparticles formed on the nanoribbons' surface. For the Ce<sup>4+</sup> batch, an increase in CeO<sub>2</sub> nanoparticle size with increasing calcination temperature was observed.

Modification of the composition of HTiNRs with Ce<sup>4+</sup> and Ce<sup>3+</sup> significantly raised the temperature for the conversion of H<sub>2</sub>Ti<sub>3</sub>O<sub>7</sub> to TiO<sub>2</sub>-B, TiO<sub>2</sub>-B to anatase, and anatase to rutile for at least 200 °C. The nanoribbon morphology remained preserved up to 860 °C. Anatase to rutile transformation at 960 °C caused fragmentation of the nanoribbons. In the case of the Ce<sup>3+</sup> source, at 960 °C, a smaller amount of anatase is converted to rutile. However, the cerium content was about 10 times lower than in the Ce<sup>4+</sup> sample that calcined at the same temperature, suggesting that cerium atoms occupied positions that prevented the transformation to rutile.

For the Ce<sup>4+</sup>-batch, the EELS and XPS result showed that Ce<sup>3+</sup> was present in the impregnated HTiNRs, and that the relative amount of Ce<sup>4+</sup> increased with an increasing calcination temperature. The presence of cerium in calcined products caused a decrease in the band gap energy.

**Supplementary Materials:** The following supporting information can be downloaded at: <https://www.mdpi.com/article/10.3390/molecules28155838/s1>, Figure S1: SEM image of H<sub>2</sub>Ti<sub>3</sub>O<sub>7</sub> nanoribbons (HTiNRs) used as a precursor for wet impregnation/intercalation with Ce<sup>4+</sup> and Ce<sup>3+</sup>; Figure S2: XRD of pristine HTiNRs and products calcined at 620, 750, 860, and 960 °C in air; Figure S3: XRD patterns of HTiNRs (top), Ce<sup>4+</sup>-HTiNRs (middle), and Ce<sup>3+</sup>-HTiNRs (bottom) between 7 and 15°. Vertical lines guide the eye to easily observe the (100) peak shift to higher angles for Ce<sup>3+</sup>-HTiNRs; Figure S4: SEM image of HTiNRs impregnated with Ce<sup>4+</sup> (Ce<sup>4+</sup>-HTiNRs); Figure S5: TGA curves for HTiNRs impregnated with Ce<sup>4+</sup> (Ce<sup>4+</sup>-HTiNRs) and Ce<sup>3+</sup> (Ce<sup>3+</sup>-HTiNRs) measured in air; Figure S6: TGA curve of Ce(SO<sub>4</sub>)<sub>2</sub>·4H<sub>2</sub>O measured in air and MS of H<sub>2</sub>O, SO, and SO<sub>2</sub>; Figure S7: TGA and DSC curves of Ce(NO<sub>3</sub>)<sub>3</sub>·6H<sub>2</sub>O measured in air. Figure S8: Breakdown of the nanoribbon morphology with increasing calcination temperature for Ce<sup>4+</sup>-HTiNRs calcined at **a** 620 °C, **b** 750 °C, **c** 860 °C, and **d** 960 °C. TEM images were taken at the same magnification; Figure S9: Collapse of the nanoribbon morphology with increasing calcination temperatures for HTiNRs calcined at 620 °C, 750 °C, 860 °C, and 960 °C. SEM images were taken at the same magnification with a secondary electron detector; Figure S10: CeO<sub>2</sub> NPs size distribution for Ce<sup>4+</sup>-860 °C and Ce<sup>4+</sup>-960 °C; Figure S11: STEM-EDX elemental mapping of Ce<sup>4+</sup>-620 °C. References [65,66] are cited in the Supplementary Materials.

**Author Contributions:** Conceptualization, P.U.; methodology, P.U. and C.B.; validation, P.U., C.B. and R.C.K.; formal analysis, P.U., C.B., S.Š., R.C.K., M.D. and L.M.-L.; investigation, P.U., C.B., S.Š., R.C.K., M.D. and L.M.-L.; resources, P.U., C.B. and L.M.-L.; data curation, P.U. and C.B.; writing—original draft preparation, P.U. and C.B.; writing—review and editing, P.U., C.B., S.Š., M.D. and L.M.-L.; visualization, P.U. and C.B.; supervision, P.U. and C.B.; project administration, P.U., C.B. and L.M.-L.; funding acquisition, P.U. and C.B. All authors have read and agreed to the published version of the manuscript.

**Funding:** This research was funded by Slovenian Research and Innovation Agency, through the Research Program P1-0125. C.B. is a Research Associate of the FRS-FNRS, Belgium.

**Institutional Review Board Statement:** Not applicable.

**Informed Consent Statement:** Not applicable.

**Data Availability Statement:** The data presented in this study are available on request from the corresponding author.

**Acknowledgments:** P.U. would like to acknowledge the support provided by the Slovenian Research and Innovation Agency (research program P1-0125).

**Conflicts of Interest:** The authors declare no conflict of interest.

**Sample Availability:** Not applicable.

## References

1. Diebold, U. The surface science of titanium dioxide. *Surf. Sci. Rep.* **2003**, *48*, 53–229. [[CrossRef](#)]
2. Parrino, F.; Francesca, R.P.; Giovanni, C.-R.; Vittorio, L.; Leonardo, P. 2—Properties of Titanium Dioxide. In *Titanium Dioxide (TiO<sub>2</sub>) and Its Applications*; Francesco, P., Leonardo, P., Eds.; Elsevier: Amsterdam, The Netherlands, 2021; pp. 13–66.
3. Rahimi, N.; Randolph, A.P.; Evan, M.G. Review of Functional Titanium Oxides. I: TiO<sub>2</sub> and Its Modifications. *Prog. Solid State Chem.* **2016**, *44*, 86–105. [[CrossRef](#)]
4. Wu, X. Applications of Titanium Dioxide Materials. In *Titanium Dioxide*; Hafiz Muhammad, A., Ed.; IntechOpen: Rijeka, Croatia, 2021; Chapter 9.
5. Zhang, Y.; Jiang, Z.; Huang, J.; Lim, L.Y.; Li, W.; Deng, J.; Gong, D.; Tang, Y.; Lai, Y.; Chen, Z. Titanate and titania nanostructured materials for environmental and energy applications: A review. *RSC Adv.* **2015**, *5*, 79479–79510. [[CrossRef](#)]
6. Geetha, M.; Singh, A.K.; Asokamani, R.; Gogia, A.K. Ti based biomaterials, the ultimate choice for orthopaedic implants—A review. *Prog. Mater. Sci.* **2009**, *54*, 397–425. [[CrossRef](#)]
7. Akshaya, S.; Rowlo, P.K.; Dukle, A.; Nathanael, A.J. Antibacterial Coatings for Titanium Implants: Recent Trends and Future Perspectives. *Antibiotics* **2022**, *11*, 1719. [[CrossRef](#)]
8. Wang, J.; Sun, H.; Huang, J.; Li, Q.; Yang, J. Band Structure Tuning of TiO<sub>2</sub> for Enhanced Photoelectrochemical Water Splitting. *J. Phys. Chem. C* **2014**, *118*, 7451–7457. [[CrossRef](#)]
9. Manchwari, S.; Khatter, J.; Chauhan, R.P. Modifications in structural, morphological and optical properties of TiO<sub>2</sub> nanoparticles: Effect of pH. *Chem. Pap.* **2022**, *76*, 7545–7551. [[CrossRef](#)]
10. Jian, Z.; Pu, Y.; Fang, J.; Ye, Z. Microemulsion Synthesis of Nanosized TiO<sub>2</sub> Particles Doping with Rare-Earth and their Photocatalytic Activity. *Photochem. Photobiol.* **2010**, *86*, 1016–1021. [[CrossRef](#)]
11. Wang, J.; Wang, Z.; Wang, W.; Wang, Y.; Hu, X.; Liu, J.; Gong, X.; Miao, W.; Ding, L.; Li, X.; et al. Synthesis, modification and application of titanium dioxide nanoparticles: A review. *Nanoscale* **2022**, *14*, 6709–6734. [[CrossRef](#)]
12. Chen, X.; Mao, S.S. Titanium Dioxide Nanomaterials: Synthesis, Properties, Modifications, and Applications. *Chem. Rev.* **2007**, *107*, 2891–2959. [[CrossRef](#)]
13. Irshad, M.A.; Nawaz, R.; Rehman, M.Z.u.; Adrees, M.; Rizwan, M.; Ali, S.; Ahmad, S.; Tasleem, S. Synthesis, characterization and advanced sustainable applications of titanium dioxide nanoparticles: A review. *Ecotoxicol. Environ. Saf.* **2021**, *212*, 111978. [[CrossRef](#)]
14. Zhao, Z.; Tian, J.; Sang, Y.; Cabot, A.; Liu, H. Structure, Synthesis, and Applications of TiO<sub>2</sub> Nanobelts. *Adv. Mater.* **2015**, *27*, 2557–2582. [[CrossRef](#)] [[PubMed](#)]
15. Rutar, M.; Rozman, N.; Pregelj, M.; Bittencourt, C.; Cerc Korošec, R.; Sever Škapin, A.; Mrzel, A.; Škapin, S.D.; Umek, P. Transformation of hydrogen titanate nanoribbons to TiO<sub>2</sub> nanoribbons and the influence of the transformation strategies on the photocatalytic performance. *Beilstein J. Nanotechnol.* **2015**, *6*, 831–844. [[CrossRef](#)] [[PubMed](#)]
16. Bavykin, D.V.; Friedrich, J.M.; Walsh, F.C. Protonated Titanates and TiO<sub>2</sub> Nanostructured Materials: Synthesis, Properties, and Applications. *Adv. Mater.* **2006**, *18*, 2807–2824. [[CrossRef](#)]
17. Khlyustova, A.; Sirotkin, N.; Kusova, T.; Kraev, A.; Titov, V.; Agafonov, A. Doped TiO<sub>2</sub>: The effect of doping elements on photocatalytic activity. *Mater. Adv.* **2020**, *1*, 1193–1201. [[CrossRef](#)]
18. Fang, J.; Bao, H.; He, B.; Wang, F.; Si, D.; Jiang, Z.; Pan, Z.; Wei, S.; Huang, W. Interfacial and Surface Structures of CeO<sub>2</sub>–TiO<sub>2</sub> Mixed Oxides. *J. Phys. Chem. C* **2007**, *111*, 19078–19085. [[CrossRef](#)]
19. Artiglia, L.; Agnoli, S. Cerium Oxide Nanostructures on Titania: Effect of the Structure and Stoichiometry on the Reactivity Toward Ethanol Oxidation. *J. Phys. Chem. C* **2018**, *122*, 20809–20816. [[CrossRef](#)]
20. Gionco, C.; Paganini, M.C.; Agnoli, S.; Reeder, A.E.; Giamello, E. Structural and spectroscopic characterization of CeO<sub>2</sub>–TiO<sub>2</sub> mixed oxides. *J. Mater. Chem. A* **2013**, *1*, 10918–10926. [[CrossRef](#)]
21. Kočí, K.; Matějová, L.; Ambrožová, N.; Šihor, M.; Troppová, I.; Čapek, L.; Kotarba, A.; Kustrowski, P.; Hospodková, A.; Obalová, L. Optimization of cerium doping of TiO<sub>2</sub> for photocatalytic reduction of CO<sub>2</sub> and photocatalytic decomposition of N<sub>2</sub>O. *J. Sol-Gel Sci. Technol.* **2016**, *78*, 550–558. [[CrossRef](#)]
22. Veziroglu, S.; Röder, K.; Gronenberg, O.; Vahl, A.; Polonskyi, O.; Strunskus, T.; Rubahn, H.-G.; Kienle, L.; Adam, J.; Fiutowski, J.; et al. Cauliflower-like CeO<sub>2</sub>–TiO<sub>2</sub> hybrid nanostructures with extreme photocatalytic and self-cleaning properties. *Nanoscale* **2019**, *11*, 9840–9844. [[CrossRef](#)]
23. Luo, S.; Nguyen-Phan, T.-D.; Johnston-Peck, A.C.; Barrio, L.; Sallis, S.; Arena, D.A.; Kundu, S.; Xu, W.; Piper, L.F.J.; Stach, E.A.; et al. Hierarchical Heterogeneity at the CeO<sub>x</sub>–TiO<sub>2</sub> Interface: Electronic and Geometric Structural Influence on the Photocatalytic Activity of Oxide on Oxide Nanostructures. *J. Phys. Chem. C* **2015**, *119*, 2669–2679. [[CrossRef](#)]

24. Johnston-Peck, A.C.; Senanayake, S.D.; Plata, J.J.; Kundu, S.; Xu, W.; Barrio, L.; Graciani, J.; Sanz, J.F.; Navarro, R.M.; Fierro, J.L.G.; et al. Nature of the Mixed-Oxide Interface in Ceria–Titania Catalysts: Clusters, Chains, and Nanoparticles. *J. Phys. Chem. C* **2013**, *117*, 14463–14471. [[CrossRef](#)]
25. Feist, T.P.; Davies, P.K. The soft chemical synthesis of TiO<sub>2</sub> (B) from layered titanates. *J. Solid State Chem.* **1992**, *101*, 275–295. [[CrossRef](#)]
26. Zhu, H.Y.; Lan, Y.; Gao, X.P.; Ringer, S.P.; Zheng, Z.F.; Song, D.Y.; Zhao, J.C. Phase Transition between Nanostructures of Titanate and Titanium Dioxides via Simple Wet-Chemical Reactions. *J. Am. Chem. Soc.* **2005**, *127*, 6730–6736. [[CrossRef](#)]
27. Kiatkittipong, K.; Scott, J.; Amal, R. Hydrothermally Synthesized Titanate Nanostructures: Impact of Heat Treatment on Particle Characteristics and Photocatalytic Properties. *ACS Appl. Mater. Interfaces* **2011**, *3*, 3988–3996. [[CrossRef](#)]
28. Qamar, M.; Yoon, C.R.; Oh, H.J.; Kim, D.H.; Jho, J.H.; Lee, K.S.; Lee, W.J.; Lee, H.G.; Kim, S.J. Effect of post treatments on the structure and thermal stability of titanate nanotubes. *Nanotechnology* **2006**, *17*, 5922. [[CrossRef](#)]
29. Opra, D.P.; Gnedenkov, S.V.; Sokolov, A.A.; Podgorbunsky, A.B.; Ustinov, A.Y.; Mayorov, V.Y.; Kuryavyi, V.G.; Sinebryukhov, S.L. Vanadium-doped TiO<sub>2</sub>-B/anatase mesoporous nanotubes with improved rate and cycle performance for rechargeable lithium and sodium batteries. *J. Mater. Sci. Technol.* **2020**, *54*, 181–189. [[CrossRef](#)]
30. Uesugi, Y.; Nagakawa, H.; Nagata, M. Highly Efficient Photocatalytic Degradation of Hydrogen Sulfide in the Gas Phase Using Anatase/TiO<sub>2</sub>(B) Nanotubes. *ACS Omega* **2022**, *7*, 11946–11955. [[CrossRef](#)]
31. Liu, X.; Sun, Q.; Ng, A.M.C.; Djurišić, A.B.; Xie, M.; Liao, C.; Shih, K.; Vranješ, M.; Nedeljković, J.M.; Deng, Z. In situ synthesis of TiO<sub>2</sub>(B) nanotube/nanoparticle composite anode materials for lithium ion batteries. *Nanotechnology* **2015**, *26*, 425403. [[CrossRef](#)]
32. Huang, J.P.; Yuan, D.D.; Zhang, H.Z.; Cao, Y.L.; Li, G.R.; Yang, H.X.; Gao, X.P. Electrochemical sodium storage of TiO<sub>2</sub>(B) nanotubes for sodium ion batteries. *RSC Adv.* **2013**, *3*, 12593–12597. [[CrossRef](#)]
33. Liu, Z.; Andreev, Y.G.; Robert Armstrong, A.; Brutti, S.; Ren, Y.; Bruce, P.G. Nanostructured TiO<sub>2</sub>(B): The effect of size and shape on anode properties for Li-ion batteries. *Prog. Nat. Sci. Mater. Int.* **2013**, *23*, 235–244. [[CrossRef](#)]
34. Zhang, W.; Zhang, Y.; Yu, L.; Wu, N.-L.; Huang, H.; Wei, M. TiO<sub>2</sub>-B nanowires via topological conversion with enhanced lithium-ion intercalation properties. *J. Mater. Chem. A* **2019**, *7*, 3842–3847. [[CrossRef](#)]
35. Armstrong, A.R.; Armstrong, G.; Canales, J.; Bruce, P.G. TiO<sub>2</sub>-B Nanowires. *Angew. Chem. Int. Ed.* **2004**, *43*, 2286–2288. [[CrossRef](#)]
36. Umek, P.; Bittencourt, C.; Guttman, P.; Gloter, A.; Škapin, S.D.; Arčon, D. Mn<sup>2+</sup> Substitutional Doping of TiO<sub>2</sub> Nanoribbons: A Three-Step Approach. *J. Phys. Chem. C* **2014**, *118*, 21250–21257. [[CrossRef](#)]
37. Kolen'ko, Y.V.; Kovnir, K.; Gavrilov, A.I.; Garshev, A.V.; Frantti, J.; Lebedev, O.I.; Churagulov, B.R.; van Tendeloo, G.; Yoshimura, M.J.T.j.o.p.c.B. Hydrothermal synthesis and characterization of nanorods of various titanates and titanium dioxide. *J. Phys. Chem. B* **2006**, *110*, 4030–4038. [[CrossRef](#)]
38. Hanaor, D.A.H.; Sorrell, C.C. Review of the anatase to rutile phase transformation. *J. Mater. Sci.* **2011**, *46*, 855–874. [[CrossRef](#)]
39. Xu, D.; Li, J.; Yu, Y.; Li, J. From titanates to TiO<sub>2</sub> nanostructures: Controllable synthesis, growth mechanism, and applications. *Sci. China Chem.* **2012**, *55*, 2334–2345. [[CrossRef](#)]
40. Wen, P.; Ishikawa, Y.; Itoh, H.; Feng, Q. Topotactic Transformation Reaction from Layered Titanate Nanosheets into Anatase Nanocrystals. *J. Phys. Chem. C* **2009**, *113*, 20275–20280. [[CrossRef](#)]
41. Akimoto, J.; Chiba, K.; Kijima, N.; Hayakawa, H.; Hayashi, S.; Gotoh, Y.; Idemoto, Y. Soft-Chemical Synthesis and Electrochemical Property of H<sub>2</sub>Ti<sub>12</sub>O<sub>25</sub> as a Negative Electrode Material for Rechargeable Lithium-Ion Batteries. *J. Electrochem. Soc.* **2011**, *158*, A546. [[CrossRef](#)]
42. Sluban, M.; Umek, P. Role of Water in the Transformation of Protonated Titanate Nanoribbons to Anatase Nanoribbons. *J. Phys. Chem. C* **2019**, *123*, 23747–23757. [[CrossRef](#)]
43. Gao, Y.; Li, Z.; Su, K.; Cheng, B. Excellent performance of TiO<sub>2</sub>(B) nanotubes in selective transesterification of DMC with phenol derivatives. *Chem. Eng. J.* **2016**, *301*, 12–18. [[CrossRef](#)]
44. Viana, B.C.; Ferreira, O.P.; Souza Filho, A.G.; Rodrigues, C.M.; Moraes, S.G.; Mendes Filho, J.; Alves, O.L. Decorating Titanate Nanotubes with CeO<sub>2</sub> Nanoparticles. *J. Phys. Chem. C* **2009**, *113*, 20234–20239. [[CrossRef](#)]
45. Marques, T.M.F.; Ferreira, O.P.; da Costa, J.A.P.; Fujisawa, K.; Terrones, M.; Viana, B.C. Study of the growth of CeO<sub>2</sub> nanoparticles onto titanate nanotubes. *J. Phys. Chem. Solids* **2015**, *87*, 213–220. [[CrossRef](#)]
46. Gu, X.; Chen, F.; Zhao, B.; Zhang, J. Photocatalytic reactivity of Ce-intercalated layered titanate prepared with a hybrid method based on ion-exchange and thermal treatment. *Superlattices Microstruct.* **2011**, *50*, 107–118. [[CrossRef](#)]
47. De Santis, S.; Sotgiu, G.; Porcelli, F.; Marsotto, M.; Iucci, G.; Orsini, M. A Simple Cerium Coating Strategy for Titanium Oxide Nanotubes' Bioactivity Enhancement. *Nanomaterials* **2021**, *11*, 445. [[CrossRef](#)] [[PubMed](#)]
48. Li, N.; Zhang, L.; Chen, Y.; Fang, M.; Zhang, J.; Wang, H. Highly Efficient, Irreversible and Selective Ion Exchange Property of Layered Titanate Nanostructures. *Adv. Funct. Mater.* **2012**, *22*, 835–841. [[CrossRef](#)]
49. Shannon, R.D. Revised effective ionic radii and systematic studies of interatomic distances in halides and chalcogenides. *Acta Crystallogr. Sect. A* **1976**, *32*, 751–767. [[CrossRef](#)]
50. Hsu, W.P.; Ronnquist, L.; Matijevic, E. Preparation and properties of monodispersed colloidal particles of lanthanide compounds. 2. Cerium(IV). *Langmuir* **1988**, *4*, 31–37. [[CrossRef](#)]
51. Aubriet, F.; Gaumet, J.-J.; de Jong, W.A.; Groenewold, G.S.; Gianotto, A.K.; McIlwain, M.E.; Van Stipdonk, M.J.; Leavitt, C.M. Cerium Oxyhydroxide Clusters: Formation, Structure, and Reactivity. *J. Phys. Chem. A* **2009**, *113*, 6239–6252. [[CrossRef](#)]

52. Ikeda-Ohno, A.; Hennig, C.; Weiss, S.; Yaita, T.; Bernhard, G. Hydrolysis of Tetravalent Cerium for a Simple Route to Nanocrystalline Cerium Dioxide: An In Situ Spectroscopic Study of Nanocrystal Evolution. *Chem. A Eur. J.* **2013**, *19*, 7348–7360. [[CrossRef](#)]
53. Briois, V.; Williams, C.E.; Dexpert, H.; Villain, F.; Cabane, B.; Deneuve, F.; Magnier, C. Formation of solid particles by hydrolysis of cerium (IV) sulphate. *J. Mater. Sci.* **1993**, *28*, 5019–5031. [[CrossRef](#)]
54. Spurr, R.A.; Myers, H. Quantitative Analysis of Anatase-Rutile Mixtures with an X-ray Diffractometer. *Anal. Chem.* **1957**, *29*, 760–762. [[CrossRef](#)]
55. Krüger, P.; Sluban, M.; Umek, P.; Guttman, P.; Bittencourt, C. Chemical Bond Modification upon Phase Transformation of TiO<sub>2</sub> Nanoribbons Revealed by Nanoscale X-ray Linear Dichroism. *J. Phys. Chem. C* **2017**, *121*, 17038–17042. [[CrossRef](#)]
56. López, T.; Rojas, F.; Alexander-Katz, R.; Galindo, F.; Balankin, A.; Buljan, A. Porosity, structural and fractal study of sol–gel TiO<sub>2</sub>–CeO<sub>2</sub> mixed oxides. *J. Solid State Chem.* **2004**, *177*, 1873–1885. [[CrossRef](#)]
57. Xu, C.; Qu, X. Cerium oxide nanoparticle: A remarkably versatile rare earth nanomaterial for biological applications. *NPG Asia Mater.* **2014**, *6*, e90. [[CrossRef](#)]
58. Wang, X.; Wang, J.; Sun, Y.; Li, K.; Shang, T.; Wan, Y. Recent advances and perspectives of CeO<sub>2</sub>-based catalysts: Electronic properties and applications for energy storage and conversion. *Front. Chem.* **2022**, *10*, 1089708. [[CrossRef](#)] [[PubMed](#)]
59. Fujishima, A.; Hashimoto, K.; Watanabe, T. *TiO<sub>2</sub> Photocatalysis: Fundamentals and Applications*; BKC: Mumbai, India, 1999.
60. Singh, M.; Taelle, B.M.; Goyal, M. Modeling of size and shape dependent band gap, dielectric constant and phonon frequency of semiconductor nanosolids. *Chin. J. Phys.* **2021**, *70*, 26–36. [[CrossRef](#)]
61. Umek, P.; Korošec, R.C.; Jančar, B.; Dominko, R.; Arčon, D. The Influence of the Reaction Temperature on the Morphology of Sodium Titanate 1D Nanostructures and Their Thermal Stability. *J. Nanosci. Nanotechnol.* **2007**, *7*, 3502–3508. [[CrossRef](#)]
62. Fortner, J.A.; Buck, E.C. The chemistry of the light rare-earth elements as determined by electron energy loss spectroscopy. *Appl. Phys. Lett.* **1996**, *68*, 3817–3819. [[CrossRef](#)]
63. Song, K.; Schmid, H.; Srot, V.; Gilardi, E.; Gregori, G.; Du, K.; Maier, J.; van Aken, P.A. Cerium reduction at the interface between ceria and yttria-stabilised zirconia and implications for interfacial oxygen non-stoichiometry. *APL Mater.* **2014**, *2*, 032104. [[CrossRef](#)]
64. Kirsch, H. *Physics of Minerals and Inorganic Materials*. Von, A.S. Marfunin. Springer-Verlag Berlin–Heidelberg–New York 1979, 340 S. mit 138 Abb. u. 50 Tab., XII, Ln. 98.–DM. *Mater. Corros.* **1980**, *31*, 155–156. [[CrossRef](#)]
65. Casari, B.M.; Langer, V. Two Ce(SO<sub>4</sub>)<sub>2</sub>·4H<sub>2</sub>O polymorphs: Crystal structure and thermal behavior. *J. Solid State Chem.* **2007**, *180*, 1616–1622. [[CrossRef](#)]
66. Strydom, C.A.; Van Vuuren, C.P.J. The thermal decomposition of cerium (III) nitrate. *J. Therm. Anal.* **1987**, *32*, 157–160. [[CrossRef](#)]

**Disclaimer/Publisher’s Note:** The statements, opinions and data contained in all publications are solely those of the individual author(s) and contributor(s) and not of MDPI and/or the editor(s). MDPI and/or the editor(s) disclaim responsibility for any injury to people or property resulting from any ideas, methods, instructions or products referred to in the content.